Science Arts & Métiers (SAM)

is an open access repository that collects the work of Arts et Métiers Institute of Technology researchers and makes it freely available over the web where possible.

This is an author-deposited version published in: https://sam.ensam.eu
Handle ID: .http://hdl.handle.net/10985/15335

To cite this version :

María D. MANRIQUE-JUÁREZ, Fabrice MATHIEU, Adrian LABORDE, Sylvain RAT, Victoria SHALABAEVA, Philippe DEMONT, Olivier THOMAS, Lionel SALMON, Thierry LEICHLE, Liviu NICU, Gábor MOLNÁR, Azzedine BOUSSEKSOU - Micromachining-Compatible, Facile Fabrication of Polymer Nanocomposite Spin Crossover Actuators - Advanced Functional Materials - Vol. 28, n°29, p.1801970-1801987 - 2018

Any correspondence concerning this service should be sent to the repository Administrator : scienceouverte@ensam.eu

Arts et Métiers Institute of Technology

Micromachining-Compatible, Facile Fabrication of Polymer Nanocomposite Spin Crossover Actuators

María D. Manrique-Juárez, Fabrice Mathieu, Adrian Laborde, Sylvain Rat, Victoria Shalabaeva, Philippe Demont, Olivier Thomas, Lionel Salmon, Thierry Leichle, Liviu Nicu, Gábor Molnár, and Azzedine Bousseksou**

$[Fe^{II}(Htrz)_2(trz)](BF_4)$ spin crossover particles of 85 nm mean size are dispersed in an SU-8 polymer matrix and spray-coated onto silicon microcantilevers. The subsequent photothermal treatment of the polymer resist leads to micrometer thick, smooth, and homogeneous coatings, which exhibit well-reproducible actuation upon the thermally induced spin transition. The actuation amplitude as a function of temperature is accurately determined by combining integrated piezoresistive detection with external optical interferometry, which allows for the assessment of the associated actuation force (9.4 mN), stress (28 MPa), strain (1.0%), and work density (140 mJ cm^{-3}) through a stratified beam model. The dynamical mechanical characterization of the films evidences an increase of the resonance frequency and a concomitant decrease of the damping in the high-temperature phase, which arises due to a combined effect of the thickness and mechanical property changes. The spray-coating approach is also successfully extended to scale up the actuators for the centimeter range on a polymer substrate providing perspectives for biomimetic soft actuators.

1. Introduction

Actuator technologies based on stimuli-responsive materials (e.g., shape memory alloys, electroactive polymers, and piezoelectric ceramics) have been investigated for several decades.[1] Driven to a large extent by the specific needs of emerging robotic,[2] biomedical[3] and micro/nanomechanical[4] technologies, the interest in such smart, active materials is still steadily growing. However, as highlighted by recent reviews,[5] current actuator materials fail to satisfy simultaneously the large number of disparate requirements in terms of strain, force, bandwidth, efficiency, durability, scaling, integration, and control for their effective deployment in these disruptive applications.

In this context, we have recently proposed to explore the technological potential of molecular spin crossover (SCO) compounds for actuating purposes.[6] These transition metal complexes are able to transduce thermal, optical, electrical, or chemical stimuli into mechanical work through the dramatic change of molecular volume, which accompanies the switching between their low-spin (LS) and high-spin (HS) electronic configurations. In particular, SCO materials have potentially very promising strain and work density characteristics and, through molecular and supramolecular design, they can provide a high degree of versatility and multifunctionality.[7]

The development of novel actuating technologies requires not only innovative materials, but also appropriate strategies for their processing, use, and performance analysis at the system level.[1] This issue of device integration remains one of the major setbacks for implementing smart molecules into technologically relevant actuators and for evaluating their real interest.[7,8] In most cases, the actuating properties of molecular materials were investigated in freestanding macroscopic objects—processed either as single crystals[6,9] or incorporated into polymers.[10] Molecular films were also deposited onto micro-electromechanical systems (MEMS) using surface chemistry[11] or thermal evaporation[12] methods. While providing a substantial step toward integrated systems, these methods are, however, best suited for fabricating nanoscale films and restricted to compounds with specific physicochemical properties.

Dr. M. D. Manrique-Juárez, Dr. S. Rat, Dr. V. Shalabaeva, Dr. L. Salmon, Dr. G. Molnár, Dr. A. Bousseksou
LCC-CNRS
Université de Toulouse
CNRS
31077 Toulouse, France
E-mail: gabor.molnar@lcc-toulouse.fr; azzedine.bousseksou@lcc-toulouse.fr
Dr. M. D. Manrique-Juárez, F. Mathieu, A. Laborde, Dr. T. Leichle, Dr. L. Nicu
LAAS-CNRS
Université de Toulouse
CNRS
31031 Toulouse, France
Prof. P. Demont
CIRIMAT
Université de Toulouse
CNRS
31062 Toulouse, France
Prof. O. Thomas
LSIS
UMR 7296
Arts et Métiers ParisTech
59046 Lille, France
The ORCID identification number(s) for the author(s) of this article can be found under https://doi.org/10.1002/adfm.201801970.

DOI: 10.1002/adfm.201801970

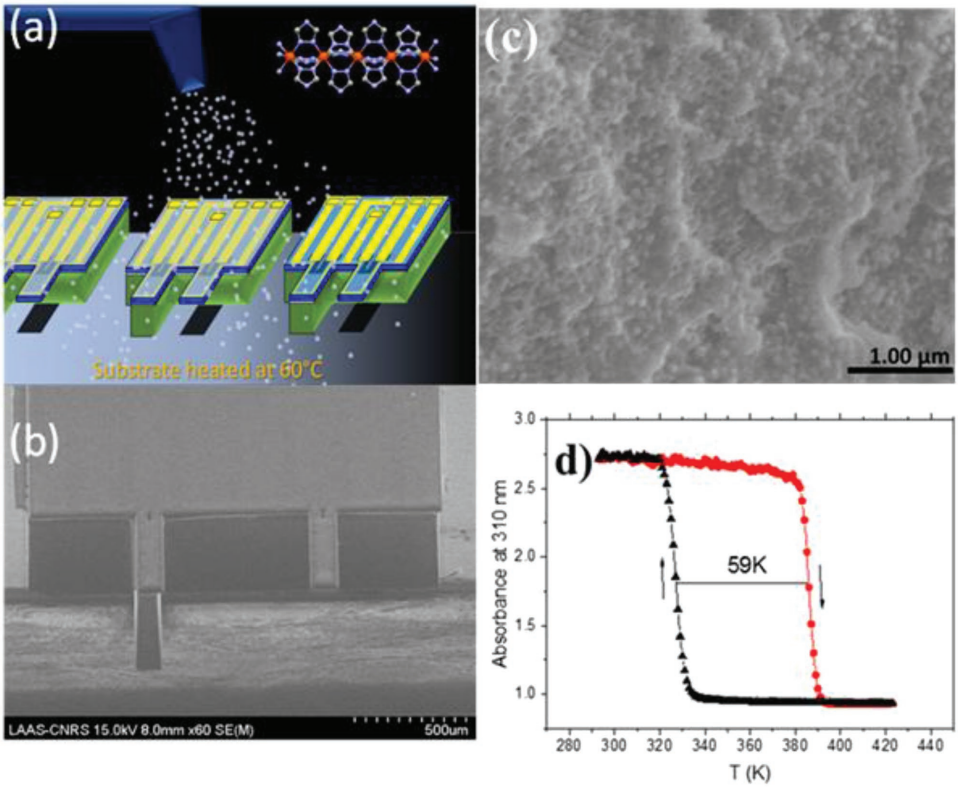

Figure 1. MEMS coating with the SCO/SU-8 composite. a) Scheme of the spray deposition on silicon cantilevers. b) SEM image of silicon cantilevers covered by the nanocomposite film. c) SEM image of the cross section of the nanocomposite film. d) UV absorbance versus temperature curve of the nanocomposite revealing the wide thermal hysteresis associated with the spin transition. Arrows indicate heating and cooling.

In this work, we explored the spray-coating technique as a versatile deposition approach to integrate spin crossover molecular actuators as polymer nanocomposites into both microscale (MEMS) and macroscopic (*sic* "artificial muscle") actuator devices. This technique consists of spraying microdroplets (i.e., an aerosol) of the desired material on a selected surface area by forcing the dissolved (or dispersed) material through a nozzle (**Figure 1**a).[13] Besides the versatility of this approach in terms of material composition and morphology, it also provides well-defined and reproducible geometries, which allowed us the quantitative investigation of the actuating performance of our SCO-based actuators in a device context.

2. Results and Discussion

2.1. Spin Crossover: Polymer Nanocomposite Films

In a first step, nanoparticles of the molecule-based SCO complex $[Fe^{II}(Htrz)_2(trz)](BF_4)$ **1** (Htrz = 1*H*-1,2,4-triazole, trz = 1,2,4-triazolato) of ≈85 nm mean size (see Figure S1 in the Supporting Information) were mixed with a commercial photoresist (SU-8) in acetone using sonication, and then were sprayed at a flow rate of 1 mL min^{-1} over heated (333 K) silicon microcantilevers. Following a prebake at 363 K, the resist was exposed to UV light and finally the crosslinking reaction was completed through further baking steps at 363 and 423 K. We have chosen **1** because this compound exhibits a very substantial volume change (≈11%) between the LS and HS isomers.[14] In addition, the spin transition in **1** is known to be very robust and occurs above room temperature with a wide hysteresis loop.[15] As polymer matrix, we used the SU-8 photoresist which is suitable for use as a permanent structure with high thermal, mechanical, and chemical stability.[16] It also provides a good adhesion to various substrates, which helps to transfer the strain from the particles to the mechanical structure. The actuating work density in composite materials is known to be strongly dependent on the filler concentration.[17] For our work, the SCO particle concentration was limited to 30 wt% in order to obtain a homogeneous dispersion of the particles in the matrix. As a future prospect for optimizing the actuating stress, we shall nevertheless investigate, in more detail, a combination of material parameters, which include size, shape, concentration, and orientation of the particles, mechanical properties of the polymer matrix, and matrix-filler interfacial properties.

Scanning electron microscopy (SEM) and atomic force microscopy (AFM) images of the spray-coated composite films revealed a smooth (arithmetic average roughness, R_a = 1 nm) and continuous surface coverage as well as a homogeneous dispersion of the particles (Figure 1b,c; see also Figures S7–S9 in the Supporting Information). The film thickness after two spraying cycles was 3.5 µm. The SCO properties of the films were inferred from UV absorbance measurements (Figure 1d; Figure S2, Supporting Information) as well as from magnetic (Figure S3, Supporting Information) and Raman spectroscopic (Figure S6, Supporting Information) measurements.

The SCO is virtually complete in both directions. The transition from the LS to the HS state occurs around 389 K ($T_{1/2}^{up}$) during the first heating, which is shifted to 386 K in the following cycles. The reverse transition (HS to LS) occurs around 327 K ($T_{1/2}^{down}$) in each cycle. The hysteresis width (≈59 K) is independent of the heating/cooling rate in the range of 1–5 K min^{-1} and, remarkably, is nearly twice as large as the hysteresis recorded for the as-synthesized particles (see Figure S4 in the Supporting Information for more details). Such an important matrix effect on the SCO properties of nanoparticles is not frequent; yet, it has already been reported on nanoparticles of **1** and other SCO compounds of different matrices.[18] This phenomenon has been—in most cases—attributed to elastic interactions with the matrix, which could not be substantiated in the present case from the vibrational spectra of our nanoparticles embedded in the SU-8 matrix (Figures S5 and S6, Supporting Information). Further investigations will thus be necessary, which are out of the scope of the present paper.

2.2. Actuating Performance

For the quantitative investigation of the mechanical and actuating properties of the nanocomposite films, we analyzed both the static and the dynamical behavior of the coated silicon microcantilevers using a home-made electrical system described in previous papers.[12] Since the cantilever is designed with a piezoresistance at the clamping zone, the static deflection induced by the expansion/contraction of the composite film triggers piezoresistance changes. For the dynamic measurements, the device was actuated at its resonance frequency by a magnetic field, and the mechanical vibrations were followed by the same piezoresistors. To quantify the amplitude of the actuation, we calibrated the piezoresistance signal using an external optical vibrometer (see the Supporting Information for more details).

To detect the actuation associated with the SCO phenomenon, the MEMSs were cycled between 293 and 423 K. As shown in **Figure 2**a, the cantilever static deflection exhibits

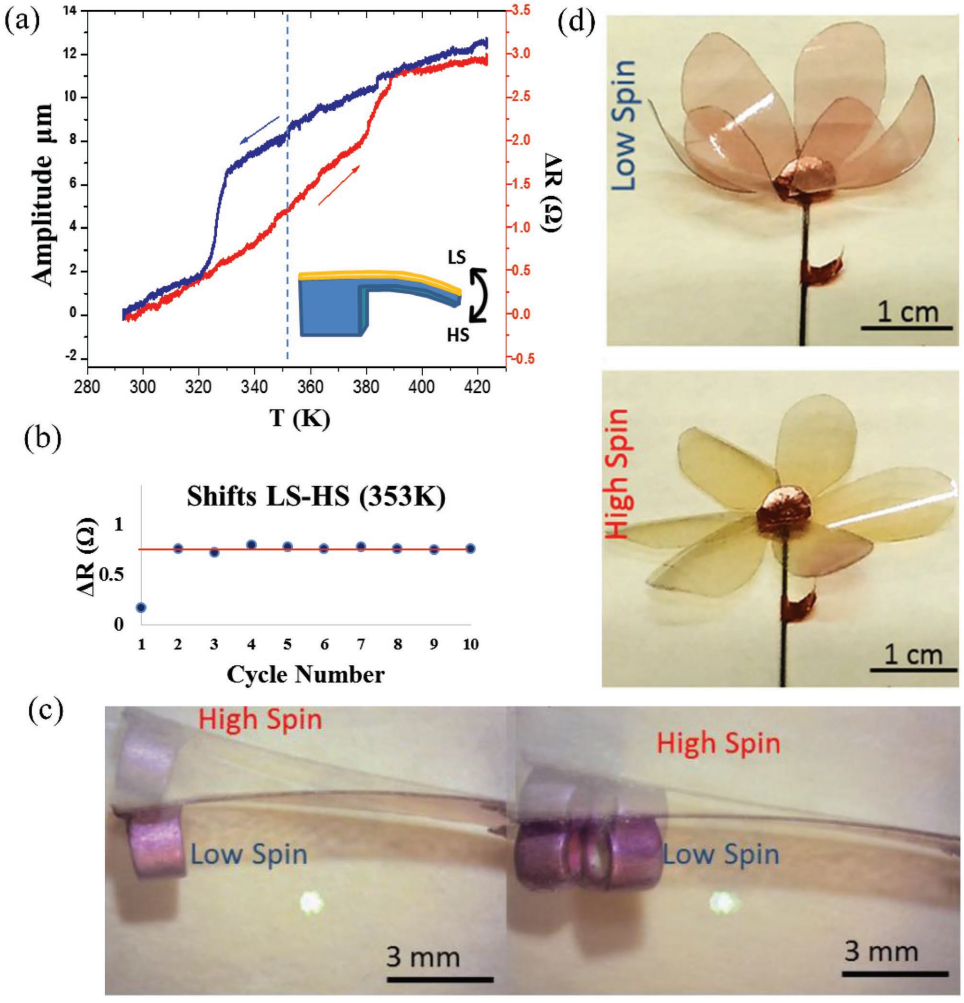

Figure 2. Actuation by SCO: from micro- to macroscopic scales. a) Temperature dependence of the static piezoresistance change and the corresponding actuation amplitude in silicon MEMS microcantilevers covered by the SCO/SU-8 composite film. Arrows indicate heating and cooling. The inset shows the deflection direction in the two spin states. b) Reproducibility of piezoresistance changes between the LS and HS states (at 353 K) upon successive thermal cycles. c) Bilayer cantilevers actuated by SCO. The attached loads (cf. purple rings) weigh 4.785 mg (left) and 9.57 mg (right). Cantilever dimensions are 11 × 2 × 0.075 mm^3. d) Artificial muscles actuated by SCO: flower closing/opening with violet/yellow coloration in the LS/HS states (see Movie S1 in the Supporting Information).

not only the gradual bending due to the thermal expansion of the device, but also very clearly the hysteresis associated with the spin transition with an abrupt downward (upward) bending around 389 K (328 K) corresponding obviously to the LS to HS (HS to LS) transitions. Overall ten thermal cycles were carried out to verify the efficiency and reproducibility of the SCO actuation in the static regime (Figure 2b). After the first cycle (run-in), the amplitude of actuation becomes stable ($\delta = 3.7 \pm 0.3$ μm). This was confirmed for two other microcantilevers (see Figure S11 in the Supporting Information) with the same thickness and width, but with different lengths (from 500 to 2810 μm), which displayed closely the same piezoresistance changes upon the SCO (0.825 ± 0.007 Ω).

To calculate the stress–strain characteristics and actuation performance of our nanocomposite film, we used a stratified beam model[19] based on classical continuum mechanics theory (see the Supporting Information for the calculation details and **Table 1** for the numerical data). The strain associated with the SCO (ε_{SCO}) was calculated by taking into account the volume fraction of the filler and the experimentally determined volume change associated with the SCO in the powder of **1**.[14] On the other hand, the measured tip displacement δ was used to calculate the curvature of the microcantilever k (see Equation (S24) in the Supporting Information). The curvature change k_{SCO} arising from the strain ε_{SCO} is described by the well-known Timoshenko formula,[20] from which the Young's modulus E of the nanocomposite film was extracted by taking into account the cantilever geometry. The strain is different in the HS → LS and LS → HS directions, corresponding to different Young's moduli in the two spin states. For the other actuation parameters, such as the volumetric and gravimetric work densities (W/V and W/m), actuating stress (σ), and blocking force (F), this difference can be neglected within the experimental uncertainty. It is important to note that the bending of the cantilever between the LS and HS states refers to the same temperature inside the hysteresis loop (353 K), i.e., no contribution arises from ordinary thermal expansion.

The most relevant actuating parameters of our device are compared with various actuator technologies (electroactive polymers, phase change materials, etc.) in **Table 2**. From this comparison we shall note the moderate strain (1.0%) and Young's modulus (3.2 GPa at 353 K), which are associated with the dilution of the SCO filler in the polymer. Yet, distinctly high values of actuation stress (28 MPa), normalized tip force (143 MPa), and work density (140 mJ cm^{-3}) are obtained for our SCO/SU-8 polymer composite material, which are comparable (or better) to the performance metrics of already mature polymer actuator materials.

2.3. Macroscopic Actuators

With the aim to scale up our actuating nanocomposite to macroscopic sizes, we have also elaborated centimeter-scale bilayer actuator devices comprising a 50 μm thick freestanding polyester film (3M 8211) on top of which was spray-coated a 22 μm thick film of the SCO composite. Either simple rectangular cantilevers or more complex, six-petal flowers were cut out from the bilayer sheets. These soft actuators were then used to generate macroscale mechanical movements—induced by the volume change of the molecular complexes upon SCO. For example, cantilevers were used to lift weight (Figure 2c), while thermal cycling of the flowers was used to mimic the reversible opening of certain flowers, such as tulip or crocus,[30] upon temperature rise (Figure 2d). To some extent even the mechanistic details resemble; in flowers the different thermal growth rates of outer and inner perianth members are thought to induce a swift mechanical effect, while in our artificial flower it is the sudden elongation of the inner SCO layer upon heating which leads to opening. A striking feature of the petal folding of the synthetic flower is the characteristic color change between violet (LS) and yellow (HS). From a biomimetic perspective, this color-changing ability coupled to motility offers potential camouflage,

Table 1. MEMS geometry and material properties.

	Si substrate	Composite film	Ref.
Length, L [μm]	840	840	Exp.
Thickness, h [μm]	20	3.50	Exp.
Width, b [μm]	100	100	Exp.
Density, ρ [kg m^{-3}]	2330	1150 (SU-8), 1984 (LS), 1778 (HS)	Ref. [14,21,22]
Young's modulus, E [GPa]	169	3.2 (LS), 2.8 (HS)	Ref. [21], Eq. 25
Actuation amplitude, δ_{SCO} [μm]		3.65	Exp.
Beam curvature, k_{SCO} [m^{-1}]		10.3	Eq. 24
Tip blocking force, F [mN]		9.4	Eq. 28a
Normalized force, F [MPa]		143	Eq. 28b
Linear strain, ε_{SCO}	N.A.	0.01 (LS→HS), 0.009(HS→LS)	Eq. 7
Volumetric work density, W/V [mJ cm^{-3}]	N.A.	140	Eq. 29a
Gravimetric work density, W/m [mJ g^{-1}]	N.A.	100	Eq. 29b
Actuating stress, σ [MPa]	N.A.	28	Eq. 8

Exp.: experimentally determined values; Eq. no.: Calculated using Equation number in the Supporting Information.

Table 2. Performance metrics of selected bending actuators from the literature.

Active material	Actuator dimension [mm]	Young's modulus [GPa]	Strain [%]	Stress [MPa]	Work density [mJ cm^{-3}]	Normalized force [MPa]	Stimulus	Ref.
Nylon	$90 \times 3 \times 0.87$	0.4	2.5	10	125	7.5	Heat	[23]
PEDOT	$6 \times 1 \times 0.018$	0.00033	0.5	*0.0017*	*0.004*	*0.02*	Voltage	[24]
Bucky gel	$8 \times 4 \times 0.465$	0.26	1.9	4.7	*45*	0.23	Voltage	[25]
PPy	$0.58 \times 0.22 \times 0.16$	0.12	*14*	*17*	*1180*	*0.54*	Voltage	[26]
Ru–sulfoxide polymer	$5 \times 1 \times 0.002$	0.02	0.105	*0.021*	0.0055	–	Light	[27]
SCO/SU-8 composite	$0.84 \times 0.1 \times 0.0235$	3.2	1	28	140	143	Heat	This work
VO_2	$0.3 \times 0.035 \times 0.0017$	140	0.32	510	810	*13*	Heat	[28]
NiTi	$0.2 \times w \times 0.002$	83	*5*	500	*25 000*	–	Heat	[29]

Values in italic have been calculated by us form the reported data. PEDOT = poly(3,4-ethylenedioxythiophene), PPy = polypyrrole.

signaling, and thermoregulatory functions,[31] while from an engineering point of view, these properties could be exploited in multifunctional, smart systems with integrated actuating, sensing, and control functions.[32]

Dynamical mechanical analysis (DMA) was used to compare the mechanical properties of the macroscopic bilayer films with the MEMS properties (**Figure 3**; see also Figures S15–S17 in the Supporting Information). The stiffness of the composite material is directly proportional to the resonance frequency f_r in MEMS (see the Supporting Information) and also to the storage modulus E' obtained with DMA. As for the energy dissipation we can compare the inverse of the quality factor ($1/Q$) obtained with the MEMS with the loss tangent ($\tan\delta$) in DMA. Overall, the micro- and macroscopic approaches are in good agreement, despite the high-temperature part of the SCO hysteresis being overlapped by a relaxation process in the polyester substrate in DMA measurements. Notably a small, but well-reproducible decrease of both f_r (Figure 3a) and E' (Figure 3c) is observed when going from the HS to the LS phase—in agreement with previous works on SCO/cellulose and SCO/polyvinylidene fluoride (PVDF) composites.[33] This finding denotes the apparent softening of the composite in the LS phase, which contrasts with the static measurements. However, one shall note that the dynamical behavior depends not only on the stiffness, but also on the sample geometry and density changes (see the Supporting Information for details on the cantilever dynamics).

The variation of $1/Q$ (Figure 3b) and $\tan\delta$ (Figure 3d) also reproduces the SCO with a clear drop in the HS phase (less damping). This decrease of internal frictions in the HS phase was also observed in SCO–PVDF composites.[33] However, in stark contrast to previous studies, no obvious loss peaks are observed at the spin transition denoting less friction in the course of the phase change.

3. Conclusions

In summary, we introduced spray coating as a facile, versatile and precise method for integrating "reluctant" molecular actuating materials as nanoparticle composites into both micrometric and macroscopic actuator devices. In particular, we succeeded in elaborating smooth, homogeneous films of nanoparticles of the molecule-based spin crossover complex $[Fe(Htrz)_2(trz)](BF_4)$ in an SU-8 polymer matrix with thicknesses in the micrometer range. Interestingly, the composite films exhibited SCO with thermal hysteresis loops twice as large as the initial nanoparticles. This effect possibly stems from the mechanical interaction with the crosslinked polymer matrix and provides scope to use these actuators in a "catch-state" (i.e., without consuming energy). Actuation of MEMS devices with the SCO/SU-8 nanocomposite films led to well-reproducible (both device-to-device and cycle-to-cycle), large actuation amplitude and stress upon the spin transition. The associated high work density (140 mJ cm^{-3}) provides the real scope for applications. Besides microsystems, we have also constructed macroscopic (centimeter scale) actuator devices based on a bilayer polymer architecture. These soft actuators displayed large deflections and perceptible color changes upon the SCO, which might be exploited in biomimetic artificial muscles.

4. Experimental Section

Synthesis of SCO Nanoparticles: An aqueous solution of $Fe(BF_4)_2{\cdot}6H_2O$ (424 mg, 1.25 mmol in 1 mL H_2O) was added dropwise to a mixture of 3.6 mL of Triton X-100, 3.6 mL pentanol, and 8 mL of cyclohexane. An identical microemulsion was prepared with a solution of H-trz (262 mg, 3.75 mmol in 1 mL H_2O). These two microemulsions were mixed together and left to stir for 24 h. The obtained nanoparticles were separated and washed three times in ethanol. The observed average diameter of the SCO nanoparticles was ≈85 nm (see Figure S1 in the Supporting Information). The particles were identified and analyzed by means of variable-temperature magnetic, optical, Raman, and infrared spectroscopic measurements, which were also used to characterize the polymer composite films (see Figures S2–S6 in the Supporting Information).

Spray-Coating Deposition of the Nanocomposite Films: A suspension of 1.4 g of EPONTM SU-8 (3050) from MicroChem Inc. and 700 mg of SCO nanoparticles in 80 g of acetone was prepared by sonication (30 min at 130 kHz). The solvent was evaporated during the deposition resulting in a charge of 30 wt% of nanoparticles inside the polymeric matrix. In parallel, control samples without nanoparticles were prepared as blank. The suspensions were deposited by a spray coater (Delta AltaSpray, SUSS MicroTec). During the deposition, the flow rate was 1 mL min^{-1}, and the substrates were kept at 60 °C to accelerate

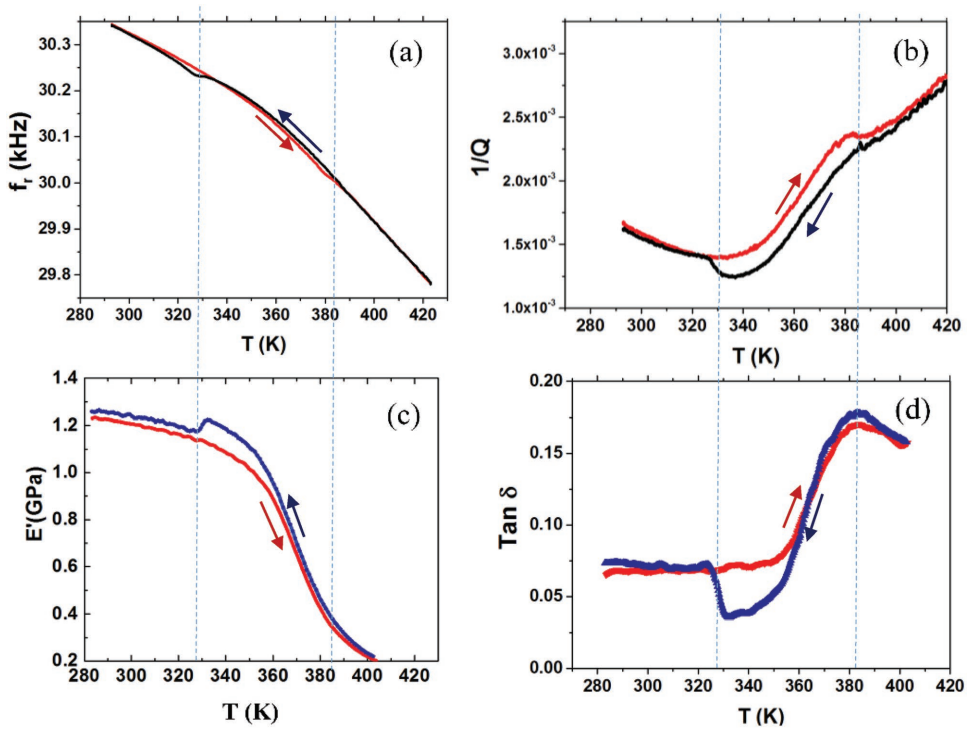

Figure 3. Dynamical mechanical properties of the SCO/SU-8 composites. Temperature dependence of the a) resonance frequency and b) reciprocal of quality factor of MEMS covered with the SCO/SU-8 composite film. Temperature dependence of the c) storage modulus and d) loss tangent of bilayer films measured by DMA. Arrows indicate heating and cooling.

the evaporation of acetone. The spray coater was designed to spray in four different directions during each cycle, which means four passes per cycle to assure a homogeneous deposition. Sub-micrometric films of ≈0.43 µm thickness were formed during each pass, and the final thickness depends on the number of deposition cycles (≈1.77 µm per cycle). After the film deposition, the sample was placed during 2 min at 363 K and then irradiated by UV light using an EVG 620 machine (90 s, 40 mW cm^{-2} at 365 nm). Finally, a postbaking at 363 K during 2 min followed by a hard baking at 423 K during 3 min was done.

Sample Characterization: The temperature-dependent (293–423 K) absorbance of the films was determined at 310 nm using a Cary 50 (Agilent Technologies) spectrophotometer and a Linkam Scientific FTIR-600 liquid nitrogen cryostat (equipped with fused silica windows). Temperature-dependent (293–423 K) white-light optical reflectance measurements were carried out using a stereomicroscope (Motic SMZ168) and a liquid nitrogen cryostat (Linkam Scientific THMS-600). Room-temperature infrared spectra were acquired in the attenuated total reflectance mode (ATR) between 4000 and 600 cm^{-1} using a Perkin Elmer Frontier FTIR spectrometer. Variable temperature Raman spectra were collected using the THMS-600 stage and an Xplora (Horiba) microspectrometer equipped with a 532 nm laser. The spectra were acquired with a resolution of ≈4 cm^{-1} in a backscattering geometry using a 50× long-working-distance objective (numerical aperture, NA = 0.5). The laser intensity on the samples was set to ≈0.15 mW. Variable-temperature magnetic susceptibility data were obtained at cooling and heating rates of 4 K min^{-1} under a field of 0.1 T using a Quantum Design MPMS superconducting quantum interference device magnetometer. The experimental data were corrected for the diamagnetic contribution. SEM images were acquired at room temperature using a Hitachi S-400 instrument. Transmission electron microscopy (TEM) images were acquired at room temperature using a JEOL JEM-1400 (200 kV) instrument. The deposited film thickness was measured using a mechanical profiler KLA-Tencor/P-15. The film roughness was measured under ambient conditions using a Cypher-ES AFM (Oxford Instruments) in tapping mode.

Mechanical Testing: An ARES G2 rheometer from TA Instruments was used to perform DMA testing using a film tension geometry. Samples were cut into a rectangular shape 24 × 7.5 mm with a thickness of 170 µm, and were loaded at a starting gap height of 10 mm. Two screw-down clamps held the film in tension while a small amplitude oscillatory strain of 0.08% was applied to it at a frequency of 1 Hz. A static axial force of 2 N on the samples was set to be at least 20% greater than the dynamic strain force applied to the film in order to prevent the sample buckling. Preliminary amplitude tests were performed at room temperature in dry nitrogen atmosphere to determine the linear viscoelastic range and optimal mechanical conditions. Data were acquired between 293 and 403 K with scan rates of 2 K min^{-1}.

MEMS Characterization: For dynamic measurements, the MEMSs were actuated at their resonance frequency using magnetic actuation and detecting the mechanical vibrations by piezoresistors. A home-built VNA card was used to track the mechanical response in terms of resonance frequency and the quality factor Q was also determined. The MEMS devices consist of a silicon chip that includes two cantilevers: one is freestanding, thus is free to bend and vibrate, while the other one is fixed to the substrate. The latter serves as a reference to offset resistance variations due to environmental changes (e.g., temperature). On the other hand, resistance variations due to cantilever deformation arise only in the freestanding structure. The electronic system has a second loop which allows compensating this variation by a modification of the polarization, which gives thus the static variation of the resistance. A Linkam Scientific HFS350EV cryostat was used to control the device temperature between 293 and 423 K at a heating/cooling rate of 2 K min^{-1}, while maintaining a constant pressure of 15 mbar during the whole experiment.

Supporting Information

Supporting Information is available from the Wiley Online Library or from the author.

Acknowledgements

This research was funded by the French RENATECH network, the Federal University of Toulouse (project IDEX Emergence NEMSCOOP), and the CNRS. M.D.M.-J. and S.R. thank the CONACYT (Grant No. 382038) and the French Ministry of Research for their Ph.D. grant. The authors thank Léa Godard (LCC) for her help with the nanoparticles' synthesis as well as Vanessa Avramovic and Sophie Eliet (IEMN, Lille) for assistance in using the optical vibrometer.

Conflict of Interest

The authors declare no conflict of interest.

Keywords

mechanical properties, micro-electromechanical systems (MEMS), nanocomposite materials, soft actuators, spin crossover complexes

Received: March 19, 2018
Revised: April 17, 2018
Published online:

[1] a) J. L. Pons, *Emerging Actuator Technologies: a Micromechatronic Approach*, Wiley, West Sussex, England **2005**; b) M. Zupan, M. F. Ashby, N. A. Fleck, *Adv. Eng. Mater.* **2002**, *4*, 933; c) J. D. W. Madden, N. A. Vandesteeg, P. A. Anquetil, P. G. A. Madden, A. Takshi, R. Z. Pytel, S. R. Lafontaine, P. A. Wieringa, I. W. Hunter, *IEEE J. Oceanic Eng.* **2004**, *29*, 706.

[2] a) *Electroactive Polymers for Robotic Applications* (Eds: K. J. Kim, S. Tadokoro), Springer-Verlag, London **2007**; b) J. D. Madden, *Science* **2007**, *318*, 1094; c) S. Kim, C. Laschi, B. Trimmer, *Trends Biotechnol.* **2013**, *31*, 287.

[3] a) *Biomedical Applications of Electroactive Polymer Actuators* (Eds: F. Carpi, E. Smela), John Wiley & Sons, West Sussex, England, **2009**; b) F. Carpi, R. Kornbluh, P. Sommer-Larsen, G. Alici, *Bioinspiration Biomimetics.* **2011**, *6*, 045006.

[4] *MEMS/NEMS Handbook, Techniques and Applications* (Ed: C. T. Leondes), Springer, Berlin **2006**.

[5] a) S. M. Mirvakili, I. W. Hunter, *Adv. Mater.* **2018**, *30*, 1704407; b) L. Hines, K. Petersen, G. Z. Lum, M. Sitti, *Adv. Mater.* **2017**, *29*, 1603483; c) *Soft Actuators* (Eds: K. Asaka, H. Okuzaki), Springer, Tokyo, Japan, **2014**; d) L. Ionov, *Langmuir* **2015**, *31*, 5015.

[6] H. J. Shepherd, I. A. Gural'skiy, C. M. Quintero, S. Tricard, L. Salmon, G. Molnár, A. Bousseksou, *Nat. Commun.* **2013**, *4*, 2607.

[7] a) M. D. Manrique-Juárez, S. Rat, L. Salmon, G. Molnár, C. M. Quintero, L. Nicu, H. J. Shepherd, A. Bousseksou, *Coord. Chem. Rev.* **2016**, *308*, 395; b) G. Molnar, S. Rat, L. Salmon, W. Nicolazzi, A. Bousseksou, *Adv. Mater.* **2018**, *30*, 17003862.

[8] a) W. R. Browne, B. L. Feringa, *Nat. Nanotechnol.* **2006**, *1*, 25; b) A. Coskun, M. Banaszak, R. D. Astumian, J. F. Stoddart, B. A. Grzybowski, *Chem. Soc. Rev.* **2012**, *41*, 19; c) F. Niess, V. Duplan, J.-P. Sauvage, *Chem. Lett.* **2014**, *43*, 964; d) J. M. Abendroth, O. S. Bushuyev, P. S. Weiss, C. J. Barrett, *ACS Nano* **2015**, *9*, 7746; e) M. A. McEvoy, N. Correll, *Science* **2015**, *347*, 1261689.

[9] a) M. Morimoto, M. Irie, *J. Am. Chem. Soc.* **2010**, *132*, 14172; b) H. Koshima, N. Ojima, H. Uchimoto, *J. Am. Chem. Soc.* **2009**, *131*, 6890; c) T. Kim, L. Zhu, R. O. Al-Kaysi, C. J. Bardeen, *ChemPhysChem* **2014**, *15*, 400.

[10] a) F. Agolini, F. P. Gay, *Macromolecules* **1970**, *3*, 349; b) H. Finkelmann, E. Nishikawa, G. G. Pereira, M. Warner, *Phys. Rev. Lett.* **2001**, *87*, 015501; c) H. Yu, T. Ikeda, *Adv. Mater.* **2011**, *23*, 2149; d) A. Goujon, T. Lang, G. Mariani, E. Moulin, G. Fuks, J. Raya, E. Buhler, N. Giuseppone, *J. Am. Chem. Soc.* **2017**, *139*, 14825; e) T. Ikeda, J. Mamiya, Y. Yu, *Angew. Chem., Int. Ed.* **2007**, *46*, 506; f) A. Priimagi, C. J. Barrett, A. Shishido, *J. Mater. Chem. C* **2014**, *2*, 7155; g) T. Ube, T. Ikeda, *Angew. Chem., Int. Ed.* **2014**, *53*, 10290.

[11] a) T. J. Huang, B. Brough, C.-M. Ho, Y. Liu, A. H. Flood, P. A. Bonvallet, H.-R. Tseng, J. F. Stoddart, M. Baller, S. Magonov, *Appl. Phys. Lett.* **2004**, *85*, 5391; b) W. Shu, D. Liu, M. Watari, C. K. Riener, T. Strunz, M. E. Welland, S. Balasubramanian, R. A. McKendry, *J. Am. Chem. Soc.* **2005**, *127*, 17054.

[12] a) M. D. Manrique-Juarez, S. Rat, F. Mathieu, D. Saya, I. Séguy, T. Leïchlé, L. Nicu, L. Salmon, G. Molnár, A. Bousseksou, *Appl. Phys. Lett.* **2016**, *109*, 061903; b) M. D. Manrique-Juárez, F. Mathieu, V. Shalabaeva, J. Cacheux, S. Rat, L. Nicu, T. Leïchlé, L. Salmon, G. Molnár, A. Bousseksou, *Angew. Chem., Int. Ed.* **2017**, *129*, 8186.

[13] C. Guirotto, B. P. Rand, J. Genoe, P. Heremans, *Sol. Energy Mater. Sol. Cells* **2009**, *93*, 454.

[14] A. Grosjean, P. Négrier, P. Bordet, C. Etrillard, D. Mondieig, S. Pechev, E. Lebraud, J.-F. Létard, P. Guionneau, *Eur. J. Inorg. Chem.* **2013**, *2013*, 796.

[15] J. Kröber, E. Codjovi, O. Kahn, F. Groliere, C. Jay, *J. Am. Chem. Soc.* **1993**, *115*, 9810.

[16] R. Feng, R. J. Farris, *J. Micromech. Microeng.* **2002**, *13*, 80.

[17] V. Q. Nguyen, A. S. Ahmed, R. V. Ramanujan, *Adv. Mater.* **2012**, *24*, 4041.

[18] a) Y. Raza, F. Volatron, S. Moldovan, O. Ersen, V. Huc, C. Martini, F. Brisset, A. Gloter, O. Stephan, A. Bousseksou, L. Catala, T. Mallah, *Chem. Commun.* **2011**, *47*, 11501; b) P. Durand, S. Pillet, E.-E. Bendeif, C. Carteret, M. Bouazaoui, H. El Hamzaoui, B. Capoen, L. Salmon, S. Hebert, J. Ghanbaja, L. Aranda, D. Schaniel, *J. Mater. Chem. C* **2013**, *1*, 1933; c) A. Tissot, C. Enachescu, M.-L. Boillot, *J. Mater. Chem.* **2012**, *22*, 20451.

[19] J. Ducarne, O. Thomas, J.-F. Deü, *J. Sound Vib.* **2012**, *331*, 3286.

[20] S. Timoshenko, *J. Opt. Soc. Am.* **1925**, *11*, 233.

[21] B. Kim, M. A. Hopcroft, R. N. Candler, C. M. Jha, M. Agarwal, R. Melamud, S. A. Chandorkar, G. Yama, T. W. Kenny, *J. Microelectromech. Syst.* **2008**, *17*, 755.

[22] MicroChem SU-8 3000 Data Sheet, http://www.microchem.com/Prod-SU83000.htm (accessed: January 2018).

[23] S. M. Mirvakili, I. W. Hunter, *Adv. Mater.* **2017**, *29*, 1604734.

[24] T. N. Nguyen, K. Rohtlaid, C. Plesse, G. T. M. Nguyen, C. Soyer, S. Grondel, E. Cattan, J. D. W. Madden, F. Vidal, *Electrochim. Acta* **2018**, *265*, 670.

[25] K. Mukai, K. Asaka, K. Kiyohara, T. Sugino, I. Takeuchi, T. Fukushima, T. Aida, *Electrochim. Acta* **2008**, *53*, 5555.

[26] G. Alici, V. Devaud, P. Renaud, G. Spinks, *J. Micromech. Microeng.* **2009**, *19*, 025017.

[27] Y. Jin, S. I. M. Paris, J. J. Rack, *Adv. Mater.* **2011**, *23*, 4312.

[28] E. Merced, X. Tan, N. Sepulveda, *Sens. Actuators, A* **2013**, *196*, 30.

[29] P. Krulevitch, A. P. Lee, P. B. Ramsey, J. C. Trevino, J. Hamilton, M. A. Northrup, *J. Micromech. Syst.* **1996**, *5*, 270.

[30] W. M. L. Wood, *J. Exp. Bot.* **1953**, *4*, 65.

[31] D. Stuart-Fox, A. Moussalli, *Philos. Trans. R. Soc., B* **2009**, *364*, 463.

[32] I. A. Anderson, T. A. Gisby, T. G. McKay, B. M. O'Brien, E. P. Calius, *J. Appl. Phys.* **2012**, *112*, 041101.

[33] a) S. Rat, V. Nagy, I. Suleimanov, G. Molnar, L. Salmon, P. Demont, L. Csoka, A. Bousseksou, *Chem. Commun.* **2016**, *52*, 11267; b) S. Rat, M. Piedrahita-Bello, L. Salmon, G. Molnar, P. Demont, A. Bousseksou, *Adv. Mater.* **2018**, *30*, 1705275.